Journal of Rock Mechanics and Geotechnical Engineering 16 (2024) 1455–1466

Contents lists available at ScienceDirect

Journal of Rock Mechanics and Geotechnical Engineering

journal homepage: www.jrmge.cn

Technical Note

Method of fabricating artificial rock specimens based on extrusion free forming (EFF) 3D printing

Xiaomeng Shi [a,b], Tingbang Deng [a,b,*], Sen Lin [a,b], Chunjiang Zou [c,**], Baoguo Liu [a,b]

[a] Key Laboratory for Urban Underground Engineering of the Ministry of Education, Beijing Jiaotong University, Beijing, 100044, China
[b] School of Civil Engineering, Beijing Jiaotong University, Beijing, 100044, China
[c] Department of Civil Engineering, Monash University, Melbourne, 3800, Australia

ARTICLE INFO

Article history:
Received 15 February 2023
Received in revised form
16 April 2023
Accepted 15 May 2023
Available online 20 July 2023

Keywords:
Artificial rock
3D printing
Extrusion free forming (EFF)
Similarity analysis
Mechanical properties

ABSTRACT

Three-dimensional (3D) printing technology has been widely used to create artificial rock samples in rock mechanics. While 3D printing can create complex fractures, the material still lacks sufficient similarity to natural rock. Extrusion free forming (EFF) is a 3D printing technique that uses clay as the printing material and cures the specimens through high-temperature sintering. In this study, we attempted to use the EFF technology to fabricate artificial rock specimens. The results show the physico-mechanical properties of the specimens are significantly affected by the sintering temperature, while the nozzle diameter and layer thickness also have a certain impact. The specimens are primarily composed of SiO_2, with mineral compositions similar to that of natural rocks. The density, uniaxial compressive strength (UCS), elastic modulus, and tensile strength of the printed specimens fall in the range of 1.65–2.54 g/cm^3, 16.46–50.49 MPa, 2.17–13.35 GPa, and 0.82–17.18 MPa, respectively. It is capable of simulating different types of rocks, especially mudstone, sandstone, limestone, and gneiss. However, the simulation of hard rocks with UCS exceeding 50 MPa still requires validation.

1. Introduction

Rock, as a geological material with a diverse range of mineral compositions and structural characteristics, presents challenges in duplicating the mechanical properties obtained through natural sampling (Pollard and Aydin, 1988; Hudson and Harrison, 1997). To overcome this challenge, researchers have attempted to fabricate artificial rocks to ensure consistent structural and mechanical characteristics within the same group of specimens. Conventional methods frequently fabricate artificial rocks by cementing rock-like materials, e.g. cement, gypsum, and quartz sand, using specific molds with different sizes and structures (Noferesti and Rao, 2010; Cao et al., 2016; Shi et al., 2018). However, due to the limitation of molds, these methods can only produce specimens with simple geometries (Zhao et al., 2016). The advancement of three-dimensional (3D) printing technologies offers a new way to fabricate artificial rock-like specimens. 3D printing allows complicated geometries or structures of the specimens with high accuracy in forming and a short production cycle (Moon et al., 2014). 3D printing has been widely utilized to fabricate standard specimens, structured surfaces, and even fractured rocks in rock mechanics, as shown in Fig. 1.

Different 3D printing materials and techniques have been applied to the fabrication of rock specimens (see Table 1). In general, the materials used for 3D printing require processability (including melting, extrusion, and jetting), adhesion, formability, physical strength, and safety. At the early stages of 3D printing rock-like samples, gypsum is used to make standard specimens as shown in Fig. 1a (Lowmunkong et al., 2009; Bobby and Singamneni, 2014). To create specimens with complicated internal structures, computerized tomography scanning technology is introduced to 3D printing to replicate micro- (pores and microcracks) and macro-structures (voids, cracks, or fillings) in rocks or rock masses as shown in Fig. 1b (Ishutov et al., 2015; Xiong et al., 2015). In recent years, the widespread use of fused deposition modeling (FDM), stereolithography appearance (SLA), and selective laser sintering (SLS) has made it easy to simulate the characteristics of joints and

* Corresponding author. Key Laboratory for Urban Underground Engineering of the Ministry of Education, Beijing Jiaotong University, Beijing, 100044, China.
** Corresponding author.
E-mail addresses: 20115017@bjtu.edu.cn (T. Deng), chunjiang.zou@monash.edu (C. Zou).

Peer review under responsibility of Institute of Rock and Soil Mechanics, Chinese Academy of Sciences.

https://doi.org/10.1016/j.jrmge.2023.05.011

(a) (b) (c)

Fig. 1. 3D printing specimens in rock mechanics: (a) Standard specimen (Jiang et al., 2016b); (b) Complex structural plane (Jiang et al., 2016a); and (c) Complex internal damage (Ju et al., 2014).

Table 1
Published cases of 3D printing in geotechnical studies.

Printed material	3D printing method	Source
Plastic	FDM	Ishutov et al. (2015)
Polylactic acid (PLA)	SLA	Xiong et al. (2015)
PLA	FDM	Jiang and Zhao (2015)
PLA and gypsum powder	3D powder-based printing (3DP) and FDM	Jiang et al. (2016a)
Gypsum powder	3DP	Jiang et al. (2016b)
Ceramics, gypsum, poly (methyl methacrylate), acrylic copolymer, resin	3DP, FDM, SLA	Zhou and Zhu (2018)
Gypsum	3DP	Song et al. (2018)
Polyamide	SLS	Zhou et al. (2020)
Gypsum	3DP	Jaber et al. (2020)
Gypsum and PLA	3DP and FDM	Jiang et al. (2021)

fractures in rock mass, as shown in Fig. 1c (Jiang and Zhao, 2015; Jiang et al., 2016a; Liu et al., 2017; Song et al., 2018; Zhou et al., 2020). Researchers have also expanded their application in rock dynamics by investigating the effect of strain rate on brittleness and failure mode, as well as the size effect (Zou et al., 2022). 3D printing is also used to create underground structures for tunnel model tests, which can be used to evaluate displacement field evolution and crack growth of surrounding rocks during tunnel construction (Song et al., 2018; Jiang et al., 2021).

However, the differences in mechanical properties and failure modes between 3D printing specimens and natural rocks limit further application of this technique. Fig. 2 illustrates the uniaxial compressive strength (UCS) and elastic modulus of typical 3D printing samples and natural rocks. The UCS value of most 3D printing specimens is less than 32 MPa. Specimens printed with silica sand and gypsum powder have a UCS value of only 4–16 MPa, approximately one-third to one-tenth that of natural sandstone (Song et al., 2020). The compressive strength of 3D printing specimens produced using the FDM method with acrylic copolymer can reach 105.6 MPa, while their corresponding elastic modulus is only one-tenth that of natural rocks (Zhou and Zhu, 2018). Concerning failure modes, the uniaxial compression failure mode of natural rocks typically involves brittle tensile failure. While the specimens made from materials, e.g. PLA, plastic, and resin (Jiang and Zhao, 2015), frequently experience plastic failure due to excessive deformation, as shown in Fig. 2c (Jiang and Zhao, 2015). In summary, while specimens produced by 3D printing currently offer significant advantages in terms of structural accuracy and repeatability, there are still notable differences in the mechanical properties and failure characteristics when compared to natural rocks.

Extrusion free forming (EFF) is a fused deposition molding technique that uses clay as raw material, prints layered structures in a specific order through a discontinuous extrusion, and cures the material through high-temperature sintering. The sintering process transforms the clay into hard ceramic, making EFF 3D printing technology suitable for producing ceramic crafts (Grida and Evans, 2003). This method has a significant potential for fabricating artificial rocks because it utilizes rock and soil materials with similar composition to natural rocks to create high-strength specimens. This study proposes a method for fabricating artificial samples for rock experiments based on EFF 3D printing technology. Numerous artificial specimens are produced using EFF 3D printing, and the physico-mechanical properties of these specimens are systematically tested. The similarities between the printed specimens and natural rocks, including mineral composition, density, strength, and stiffness, are then analyzed based on extensive data analysis.

2. Materials and method

2.1. Equipment and materials

The equipment and work procedure for EFF 3D printing are shown in Fig. 3. The 3D printer (SYNO-SOURCE-1418) consists of a 3D motion system, a motion control system, and a material delivery and extrusion molding system. The raw material used in the EFF 3D printing test is white clay soil, which is a loose or colloidal dense soil with high silicate content (e.g. porphyry and feldspar) that has undergone long-term weathering and alteration mixed with other impurities and fine minerals. The material mainly contains SiO_2, Al_2O_3, K_2O, Na_2O, Fe_2O_3, MgO, CaO, TiO_2, and a few alkali metal oxides, with SiO_2 and Al_2O_3 accounting for more than 70%. Pettijohn (1975) summarized the chemical compositions of common sedimentary rocks (see Fig. 4). The printing material has similar chemical compositions to sedimentary rocks, both of which are mainly composed of SiO_2 and Al_2O_3.

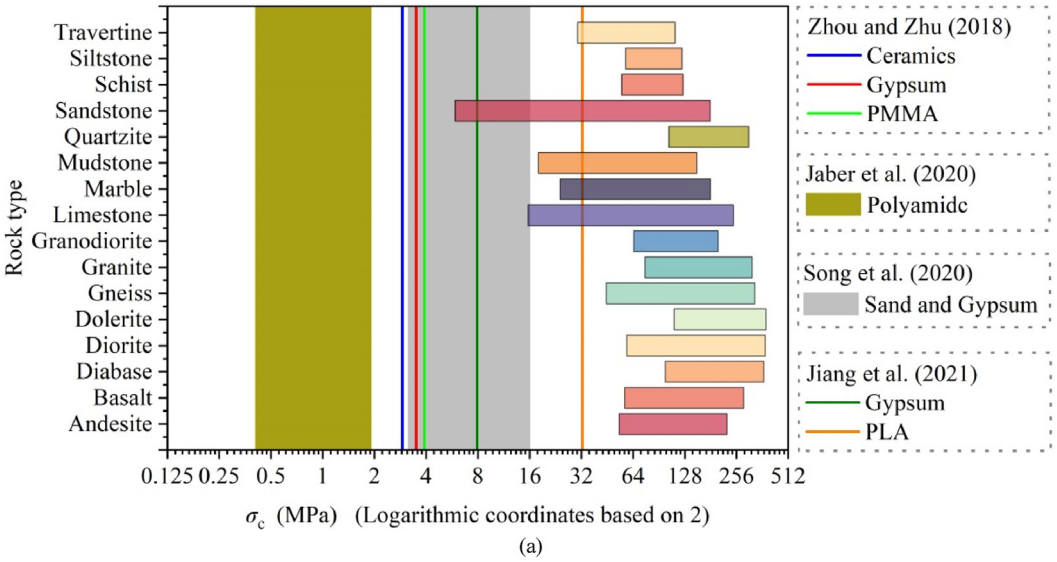

(a)

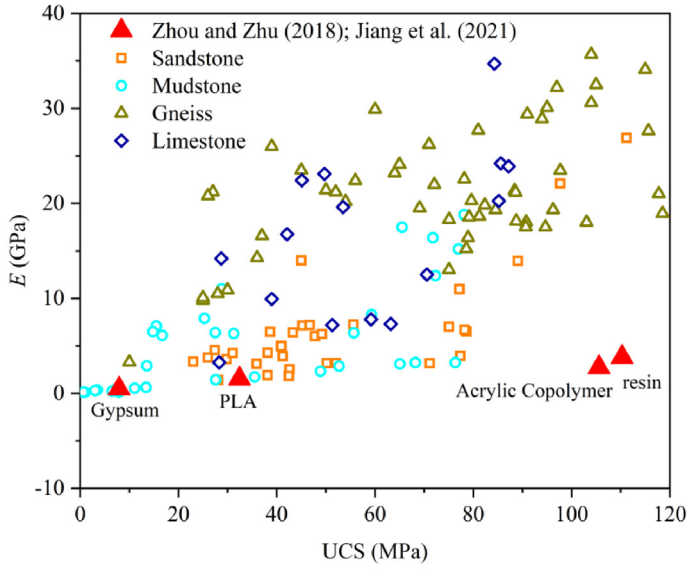

(b)

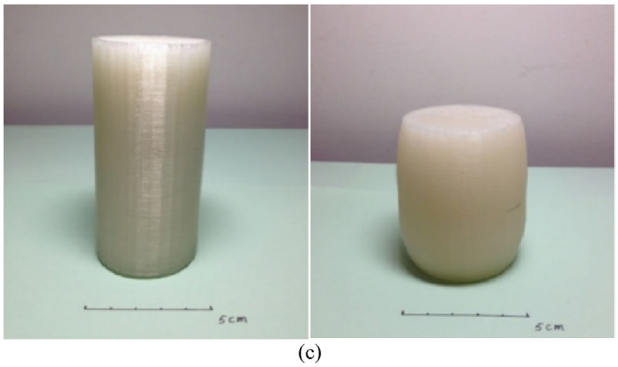

(c)

Fig. 2. Comparison between existing 3D printing rock-like materials and natural rocks. (a) UCS; (b) Elastic modulus; and (c) Failure mode of PLA specimen. (Data of 3D printing rock materials from Zhou and Zhu, 2018; Jaber et al., 2020; Song et al., 2020; Jiang et al., 2021. Data of natural rocks from Chen and Pan, 1998; Kahraman et al., 2000; Altindag, 2003; Hatheway, 2009; Agliardi et al., 2014; Tatone, 2014; Walton et al., 2015; Li et al., 2016; Rao and Singh, 2017; Wang et al., 2017; Geranmayeh Vaneghi et al., 2018; Zhang et al., 2019a, b; Aladejare, 2020; Cui and Gratchev, 2020; Du et al., 2020; Wang et al., 2020; Zhai et al., 2020; Cui et al., 2021; Liu et al., 2021; Han et al., 2022; Zhou et al., 2022). PMMA is short for polymethyl methacrylate.

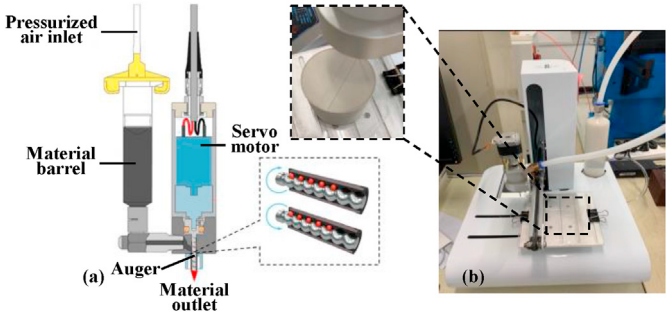

Fig. 3. EFF 3D printing (a) principle (EFD Inc., 2003) and (b) equipment (SYNO-SOURCE-1418).

2.2. Experimental design

For EFF 3D printing, the nozzle diameter D, layer thickness h, and sintering temperature T are three major parameters controlling the properties of specimens. Fang et al. (2002) proposed a uniform experimental design method to obtain sufficient data from a limited number of samples using an approach similar to orthogonal design, which utilizes the uniformity of the distribution to reduce the number of required specimens with various parameters and their values. The current study utilized three parameters with five levels to design the tests, as shown in Table 2. The ranges of nozzle diameter D, layer thickness H, and sintering temperature T are 1–1.8 mm, 0.6–1 mm, and 800 °C-1200 °C, respectively.

2.3. Specimen forming process

The fabricating process for EFF 3D printing specimens involves four steps, as shown in Fig. 5a:

(1) Creating the specimen model using the open-source software FreeCAD;
(2) Slicing the model at the horizontal plane according to the designed layer thickness using the open-source software CURA;
(3) Importing the sliced model into the 3D printer and starting the printing process after setting the printing parameters; and
(4) Sintering the printed specimen at a specific temperature.

The printed specimens must be dried in an oven at 105 °C for 24 h prior to high-temperature sintering in a muffle furnace. At the initial sintering stage (up to 300 °C), the heating rate is controlled at 3 °C/min to discharge free water and bond water from the specimens and prevent the specimen surface from cracking. After the temperature reaches 300 °C, the heating rate is increased to 5 °C/min until the maximum temperature is reached, and the temperature is then maintained for 2 h. At the final stage, the oven reduces the sintering temperature at a rate of 5 °C/min and ceases heating at 300 °C. At this point, the muffle furnace is turned off until the temperature returns to room temperature. Fig. 6 illustrates the variation in heating temperature during the sintering process.

Based on the above fabrication process and the design of printing parameters listed in Table 2, ϕ50 mm × 100 mm and ϕ50 mm × 25 mm standard specimens are produced for physico-mechanical property tests, as shown in Fig. 5b.

Table 2
Uniform test design of the EFF 3D printing parameters.

Test No.	Value		
	D (mm)	H (mm)	T (°C)
1	1	0.7	1100
2	1.2	0.9	1000
3	1.4	0.6	900
4	1.6	0.8	800
5	1.8	1	1200

2.4. Testing of mechanical properties

To evaluate the similarity of mechanical properties between the EFF specimens and natural rocks, tests are conducted to obtain critical physico-mechanical parameters including dry density ρ, UCS σ_t, elastic modulus E, and tensile strength σ_c. The values of σ_t and E are obtained using ϕ50 mm × 100 mm standard cylinders through uniaxial compression tests according to the methods suggested by Hatheway (2009). The Brazilian splitting test (BST) is used to obtain the tensile strength of ϕ50 mm × 25 mm standard disc specimens, also according to the methods suggested by Hatheway (2009), as shown in Fig. 7.

3. Experimental results

3.1. Shrinkage in the sintering process

The white clay soil used as the print material has a water content of 27%. The water improves the fluidity of the material, which is necessary for extrusion 3D printing. However, the water discharge in the drying and sintering process will induce unfavorable shrinkage in the specimen dimensions. The dimensions of each specimen are measured before and after sintering to analyze the shrinkage. The dimensional shrinkage rate η is defined by

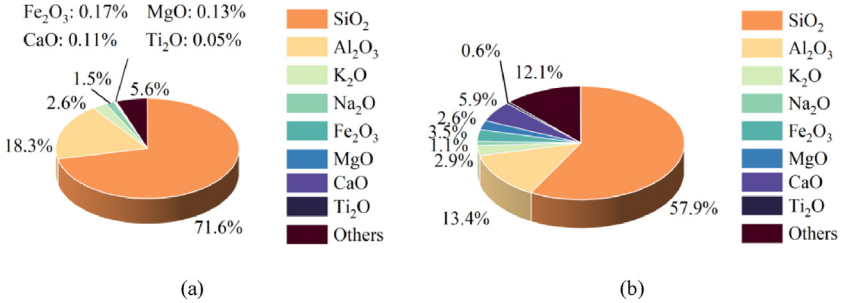

Fig. 4. Comparison of chemical composition between EFF 3D printing material and sedimentary rocks. Chemical compositions of (a) EFF 3D printing materials and (b) common sedimentary rocks (Pettijohn, 1975).

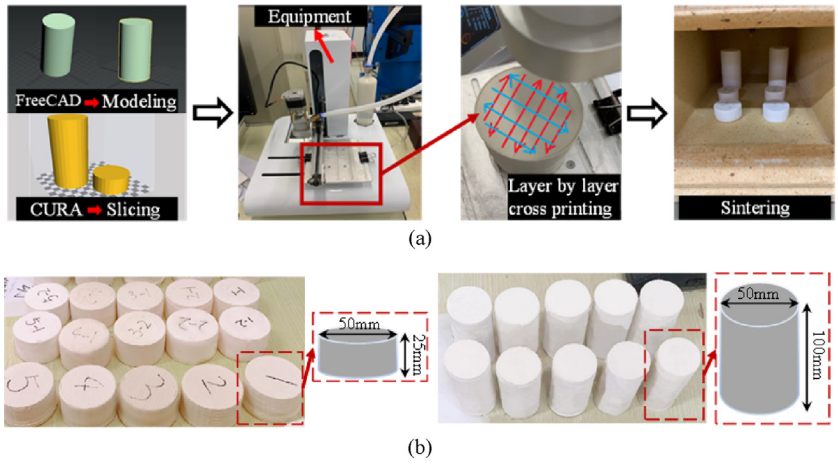

Fig. 5. (a) Forming process of EFF 3D printing; and (b) EFF 3D printing disc and cylindrical specimens.

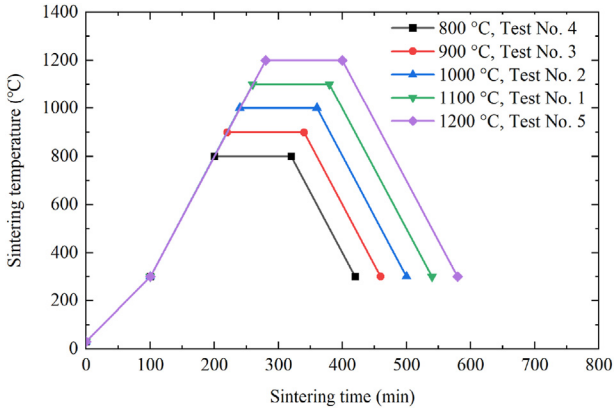

Fig. 6. Sintering temperature process.

Fig. 7. Equipment for the testing of mechanical properties: (a) Uniaxial compression test, and (b) Brazilian disc test.

$$\eta = \frac{L_0 - L_1}{L_0} \times 100\% \tag{1}$$

where L_0 is the size of a certain dimension before sintering and L_1 is the size after sintering. Table 3 lists the dimensions of these specimens before and after sintering for each test.

The results indicate that there is a certain difference between the axial and radial shrinkage rates of the specimens. Nevertheless, a minor difference is noticed. The average shrinkage rate can be used to represent the overall shrinkage situation of the specimens. The average shrinkage rate increases linearly with the sintering temperature, ranging from 9% to 18.75%. The multiple linear regression method is used to analyze the influence of multiple factors on the shrinkage rate. Based on the data in Table 3, the regression of the shrinkage rate can be obtained using

$$\eta = -17.375 - 0.375D + 0.5H + 0.03025T \tag{2}$$

The multiple linear regression model fits well with the experimental data. The correlation coefficient R of the polynomial regression equation is 0.992, and the coefficient of determination R^2 is 0.983, indicating a strong linear correlation between the dependent and independent variables. According to Eq. (2), the size change of the specimens before and after sintering can be estimated. For example, if a standard cylindrical specimen with dimensions of ϕ50 mm × 100 mm is desired under the conditions of D = 1.8 mm, H = 1 mm, and T = 1000 °C, the input print size before sintering should be ϕ57.3 mm × 114.5 mm.

3.2. Chemical component

X-ray diffraction (XRD) analysis is used to examine the mineral composition of the raw material and the specimens after heating treatment, as high-temperature treatment may alter chemical components. The XRD tests confirm the mineral composition changes with different sintering temperatures. SiO_2 is a fundamental component of rocks with a percentage of around 40%, and its stable structure results in minimal changes in content before and after sintering. Illite is the clay mineral with low strength. Feldspars are a group of rock-forming aluminum tectosilicate minerals. The compositions of illite and feldspar decrease significantly with increasing temperature. Illite disappears completely at 1000 °C, and feldspar disappears at 1100 °C. Instead, amorphous and mullite appear at 800 °C and 1000 °C, respectively, indicating the transition of mineral types after heating treatment. Amorphous or poorly crystalline materials, which may include major constituents, accessory minerals, and discrete particles dispersed in a rock, generally exhibit high strength (Rimsaite, 1979). The content of amorphous increases continuously to 44.3% at 1200 °C. Mullite is a rare silicate mineral formed during contact metamorphism of clay minerals. It appears at 900 °C and increases to 20.1% at 1200 °C. The

Table 3
Shrinkage rate of EFF specimens.

Item	Shrinkage rate									
	Test No. 1		Test No. 2		Test No. 3		Test No. 4		Test No. 5	
	ϕ50 mm × 100 mm	ϕ50 mm × 25 mm	ϕ50 mm × 100 mm	ϕ50 mm × 25 mm	ϕ50 mm × 100 mm	ϕ50 mm × 25 mm	ϕ50 mm × 100 mm	ϕ50 mm × 25 mm	ϕ50 mm × 100 mm	ϕ50 mm × 25 mm
Diameter before sintering (mm)	50.1	50.1	50.2	50	50.2	50.1	49.9	49.8	50	50
Height before sintering (mm)	100.2	24.9	100.1	25	100	25.1	99.9	24.9	100.1	25
Diameter after sintering (mm)	42.09	42.09	43.73	44.09	45	46.09	45.27	46.18	41.18	41.91
Height after sintering (mm)	82.91	20.65	88.64	21.67	92.27	22.5	93.91	23.43	80.27	19.72
Shrinkage rate of diameter (%)	16	16	13	12	10	8	9	8	18	16
Shrinkage rate of height (%)	17	17	11	13	8	10	6	6	20	21
Average shrinkage rate (%)	16.5		12.25		9		7.25		18.75	

changes in these composition percentages are shown in Fig. 8. The variation of mineral composition with temperature is consistent with the study of Ersoy et al. (2021). During the sintering process, the clay minerals undergo a transformation into amorphous and mullite with increasing temperature, resulting in increased specimen density and hardness.

3.3. Physico-mechanical properties

Table 4 shows the results of the physico-mechanical tests. The software of IBM SPSS Statistics is used to analyze the influence of the forming parameters (D, H, T, η, ρ, σ_c, σ_t, and E) on the physico-mechanical properties using the multiple linear regression method, taking into account the coupling effects of different parameters through the use of the uniform experimental design method.

Regression analysis of the experimental data in Table 4 was conducted to determine the influence of the printing parameters (i.e. nozzle diameter D, printing layer thickness H, and sintering temperature T) on the physico-mechanical properties:

$$\rho = -0.252 + 0.06D - 0.1H + 0.00232T \tag{3}$$

$$\sigma_c = -57.7345 + 0.5025D - 0.89H + 0.090175T \tag{4}$$

$$\sigma_t = -44.3655 + 7.2275D - 5.35H + 0.044905T \tag{5}$$

$$E = -21.39 + 0.32D - 1.86H + 0.03002T \tag{6}$$

The t-test can be used to analyze the significance of regression coefficients. The specific procedure entails conducting a hypothesis test, by setting the null hypothesis H_0 as $\beta_i = 0$, where β_i represents the regression coefficient. The t-value is calculated using the estimation value of the regression coefficient divided by its standard deviation. The absolute value of the calculated t-value indicates the degree of significance of the corresponding independent variable's impact on the dependent variable. As shown in Table 5, the results of the t-test indicate that the sintering temperature T has the most significant impact on the physico-mechanical properties of the printed specimens, with all of these properties showing an increasing trend with temperature. The density and strength of the specimens can be increased by

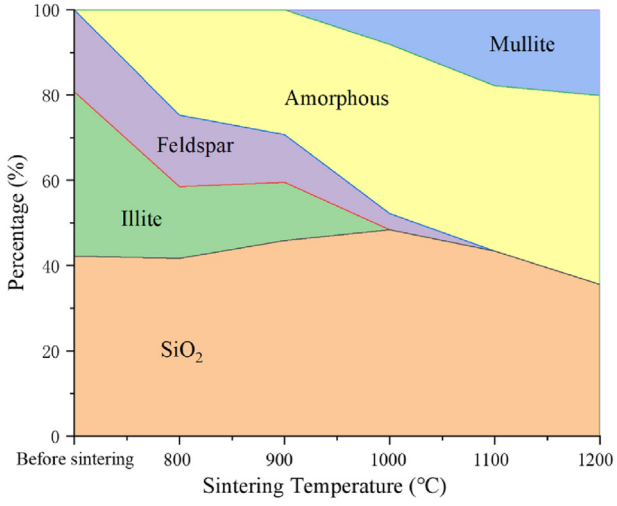

Fig. 8. Variation of the mineral compositions of the EFF specimens sintered under different temperatures.

Table 4
The physico-mechanical properties of EFF specimens.

Test No.	D (mm)	H (mm)	T (°C)	η (%)	ρ (g/cm^3)	σ_c (MPa)	σ_t (MPa)	E (GPa)
1	1	0.7	1100	16.5	2.32	43.3	10.49	11.17
2	1.2	0.9	1000	12.25	2.02	30.28	2.42	6.82
3	1.4	0.6	900	9	1.83	21.63	0.98	4.44
4	1.6	0.8	800	7.25	1.65	16.46	0.82	2.17
5	1.8	1	1200	18.75	2.54	50.49	17.18	13.35

Table 5
The t-test of multiple linear regression.

Item	t-value		
	D (nozzle diameter)	H (print layer thickness)	T (sintering temperature)
ρ	0.516	−0.373	9.984
σ_c	0.066	−0.051	5.932
σ_t	0.944	−0.302	2.932
E	0.159	−0.4	7.453

Note: The t-values are calculated by the t-test.

decreasing the print layer thickness H or increasing the nozzle diameter D. Nevertheless, the sintering temperature is the primary factor influencing the material properties, while layer thickness and nozzle diameter are secondary factors. Therefore, controlling the sintering temperature is the most important method for controlling the mechanical properties of EFF specimens. However, it should be noted that the nozzle diameter and printing layer thickness are also important factors, especially in terms of the tensile strength of the specimens. In conclusion, once the required mechanical parameters of the natural rock to be simulated are determined, adjusting the sintering temperature can be used as the main method for producing EFF specimens, while changing the nozzle diameter and printing layer thickness can be utilized as fine-tuning methods.

4. Similarity analysis between EFF specimens and natural rocks

The mechanical properties of the EFF 3D printing specimens, including failure mode, density, strength, brittleness, and stiffness, were compared with those of natural rocks using data collected from published papers. Tatone (2014) proposed that if the specific mechanical parameters of a rock material, especially the indicators of deformation and brittleness, fall within the statistical range of the corresponding indicators of natural rocks, the material can be considered similar to natural rocks. The results of the similarity analysis demonstrated the potential for using EFF 3D printing technology to create artificial rocks.

4.1. Similarity of failure mode

Fig. 9 shows the failure mode of EFF specimens and crack propagation in nature rocks observed in all EFF specimens, exhibiting characteristics of tension. This is similar to the failure mode of rocks under uniaxial compression. At sintering temperatures ranging from 800 °C to 900 °C, the crack propagation of the EFF specimen was insignificant, and both axial and radial deformations were relatively large, exhibiting significant plastic deformation similar to the failure mode of mudstone. As the temperature increased to 900 °C-1100 °C, cracks became more prominent, and the allowable axial and radial deformations of the specimens decreased. The failure mode changed from significant deformation to tension failure caused by cracks, and the failure mode became more brittle, which is similar to the failure mode of sandstone. At temperatures of 1100 °C-1200 °C, the specimens exhibited typical tensile failure with multiple cracks running through the entire specimen, similar to the failure mode of sandstone. However, for granite with high strength and brittleness, the failure mode is fragmentation due to the propagation of tensile cracks. The EFF specimen does not exhibit similar failure modes.

4.2. Similarity of density

The density of solid materials is a fundamental physical property. It was found that the density of 3D printing specimens using the EFF technique increases as the sintering temperature increases, ranging from 1.65 g/cm^3 to 2.54 g/cm^3, as shown in Fig. 10. Natural rock density can vary significantly, with values ranging from 0.75 g/cm^3 to 3.5 g/cm^3, and most common rocks, e.g. sandstone, limestone, and mudstone, have densities that are similar to those of 3D printing specimens. The range of density variation in 3D printing specimens can potentially be expanded through variations in sintering temperature. Overall, the density of EFF 3D printing specimens is comparable to that of natural rocks.

4.3. Similarity of strength

The compressive strength of EFF 3D printing specimens ranged from 16.46 MPa to 50.49 MPa, while the tensile strength ranged from 0.98 MPa to 17.18 MPa, as show in Fig. 11. The tensile and compressive strengths of EFF specimens are compared with natural rocks to assess their similarity as shown in Figs. 11 and 12. These values were found to be comparable to those of common sandstone, mudstone, marble, and limestone. However, the strength of EFF printed specimens was not sufficient to accurately simulate the properties of hard rocks.

It is easy to determine visually if a single indicator of rock-like materials falls within the statistical range of natural rocks.

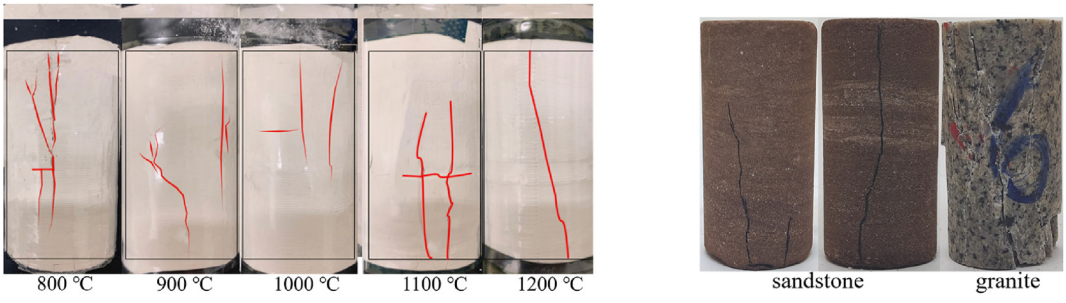

Fig. 9. Comparison of failure modes between EFF specimens and natural rocks. (a) failure mode of EFF specimens, and (b) failure mode of natural rocks.

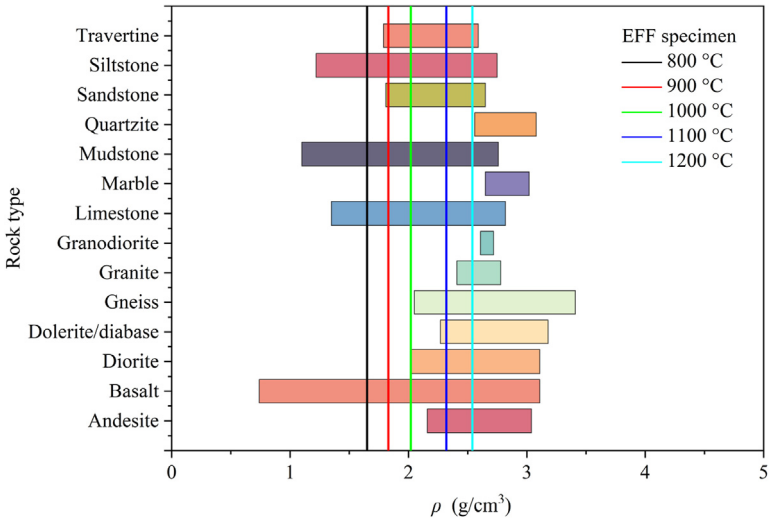

Fig. 10. Comparison of the density between EFF specimens and natural rocks (Data from Chen and Pan, 1998; Kahraman et al., 2000; Altindag, 2003; Hatheway, 2009; Agliardi et al., 2014; Tatone, 2014; Walton et al., 2015; Li et al., 2016; Rao and Singh, 2017; Wang et al., 2017; Geranmayeh Vaneghi et al., 2018; Zhang et al., 2019a, b; Aladejare, 2020; Cui and Gratchev, 2020; Du et al., 2020; Wang et al., 2020; Zhai et al., 2020; Cui et al., 2021; Liu et al., 2021; Han et al., 2022; Zhou et al., 2022).

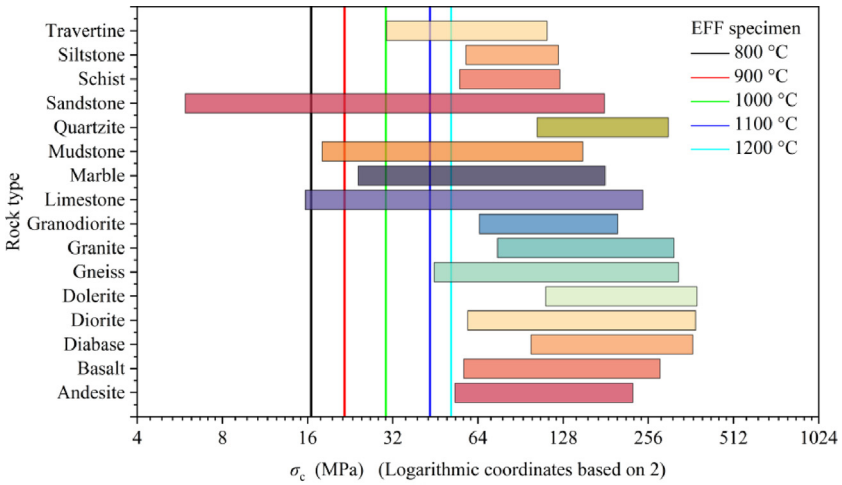

Fig. 11. Comparison of strength between EFF specimens and natural rocks. (a) compressive strength; and (b) tensile strength. (Data from Chen and Pan, 1998; Kahraman et al., 2000; Altindag, 2003; Hatheway, 2009; Agliardi et al., 2014; Tatone, 2014; Walton et al., 2015; Li et al., 2016; Rao and Singh, 2017; Wang et al., 2017; Geranmayeh Vaneghi et al., 2018; Zhang et al., 2019a, b; Aladejare, 2020; Cui and Gratchev, 2020; Du et al., 2020; Wang et al., 2020; Zhai et al., 2020; Cui et al., 2021; Liu et al., 2021; Han et al., 2022; Zhou et al., 2022).

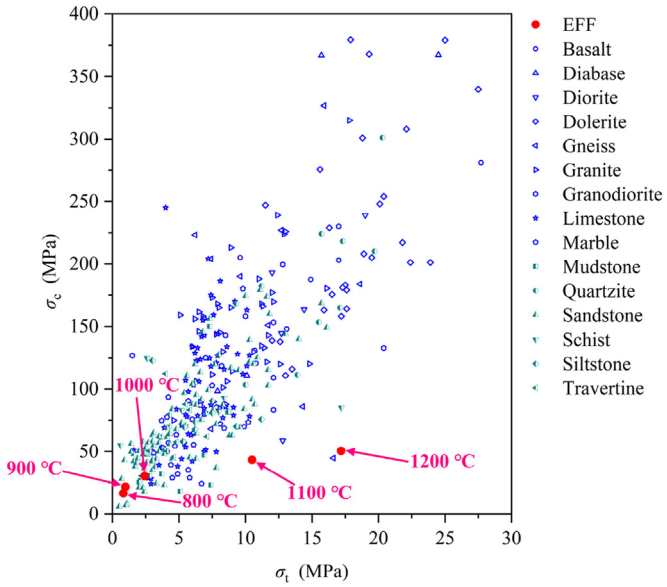

Fig. 12. Comparison of σ_c-σ_t between EFF specimens and natural rocks (Data from Chen and Pan, 1998; Kahraman et al., 2000; Altindag, 2003; Hatheway, 2009; Agliardi et al., 2014; Tatone, 2014; Walton et al., 2015; Li et al., 2016; Rao and Singh, 2017; Wang et al., 2017; Geranmayeh Vaneghi et al., 2018; Zhang et al., 2019a, b; Aladejare, 2020; Cui and Gratchev, 2020; Du et al., 2020; Wang et al., 2020; Zhai et al., 2020; Cui et al., 2021; Liu et al., 2021; Han et al., 2022; Zhou et al., 2022).

However, it is difficult to compare two indicators. This study uses colorful boxes to compare data involving two indicators. Nevertheless, this method only provides an approximate judgment and has some randomness. The density of rock is known to have a strong correlation with its strength. As shown in Fig. 13, the relationship between density and compressive strength (ρ-σ_c) and density and tensile strength (ρ-σ_t) for EFF specimens is similar to that of a variety of natural rocks, including sandstone, mudstone, limestone, and gneiss. At sintering temperatures of 800 °C-1000 °C, EFF specimens can effectively simulate low-strength mudstone. At higher sintering temperature of 1100 °C-1200 °C, EFF specimens exhibit characteristics similar to those of medium-hard sandstone, limestone, and gneiss.

4.4. Similarity of brittleness

The brittleness of a rock also plays a significant role in determining its failure mode (Zou et al., 2022), as well as its suitability for various applications, e.g. rockburst, cutting, drilling, and blasting (Dursun and Gokay, 2016; Tan et al., 2018; Yagiz et al., 2020). In order to assess the brittleness of the EFF specimens, the brittle index (B) proposed by Altindag (2010) was used in this study, which is based on the compressive and tensile strengths and is expressed by

$$B = \sqrt{\sigma_c \sigma_t} \tag{7}$$

The brittleness of natural rocks can vary significantly, ranging from 2 MPa to 128 MPa. The EFF specimens, on the other hand, have a brittleness of 3.67 MPa–29.45 MPa, which is similar to sandstone, mudstone, and limestone. This suggests that EFF specimens are suitable for simulating rocks with low brittleness, but are not suitable for rocks with high brittleness, as shown in Fig. 14.

4.5. Similarity of stiffness

The stiffness of solid materials can be analyzed through the stress-strain curve, which reflects the material's resistance to deformation under forces. The present study compared the stress-strain curves of EFF 3D printing specimens with those of natural rocks, as shown in Fig. 15. It was observed that the stiffness of EFF specimens increased with increasing sintering temperature. When sintering at temperatures ranging from 800 °C to 900 °C, the stress-strain curves of EFF specimens were relatively flat, indicating low stiffness similar to that of mudstone. At a sintering temperature of 1000 °C, the stiffness of EFF specimens was similar to that of sandstone and limestone. When the sintering temperature increased to 1100 °C–1200 °C, the stress-strain curves of EFF specimens became steeper, indicating higher stiffness similar to that of medium-hard gneiss and limestone.

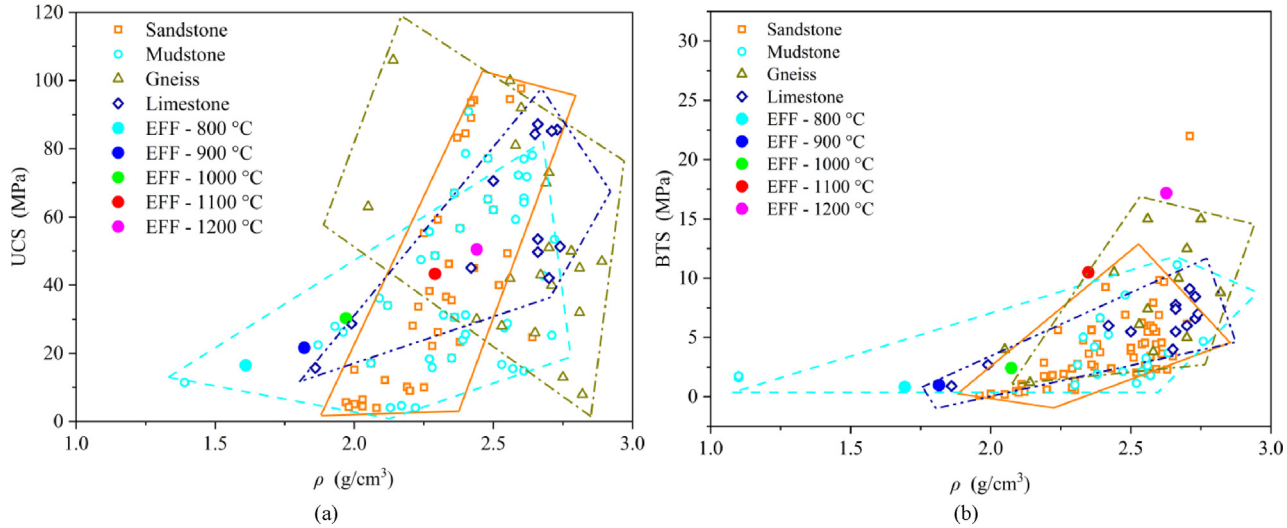

Fig. 13. Comparison of ρ-σ_c and ρ-σ_t between EFF specimens and natural rocks (a) Compressive strength; and (b) Tensile strength. (Data from Chen and Pan, 1998; Kahraman et al., 2000; Altindag, 2003; Hatheway, 2009; Agliardi et al., 2014; Tatone, 2014; Walton et al., 2015; Li et al., 2016; Rao and Singh, 2017; Wang et al., 2017; Geranmayeh Vaneghi et al., 2018; Zhang et al., 2019a, b; Aladejare, 2020; Cui and Gratchev, 2020; Du et al., 2020; Wang et al., 2020; Zhai et al., 2020; Cui et al., 2021; Liu et al., 2021; Han et al., 2022; Zhou et al., 2022).

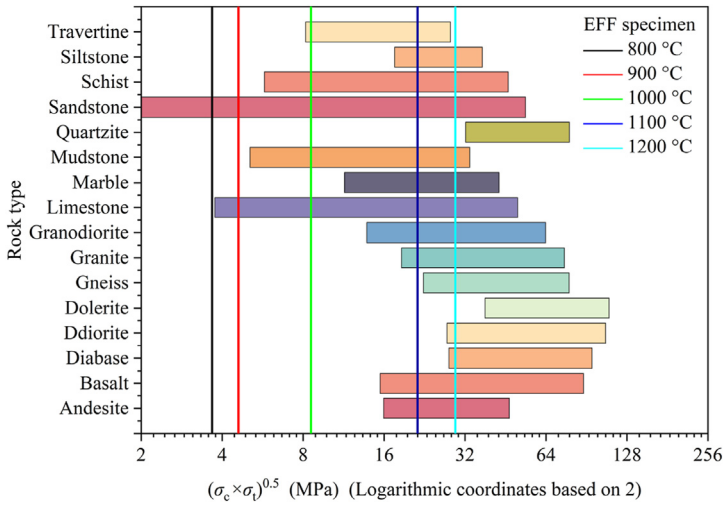

Fig. 14. Comparison of the brittleness between EFF specimens and natural rock (Data from Chen and Pan, 1998; Kahraman et al., 2000; Altindag, 2003; Hatheway, 2009; Agliardi et al., 2014; Tatone, 2014; Walton et al., 2015; Li et al., 2016; Rao and Singh, 2017; Wang et al., 2017; Geranmayeh Vaneghi et al., 2018; Zhang et al., 2019a, b; Aladejare, 2020; Cui and Gratchev, 2020; Du et al., 2020; Wang et al., 2020; Zhai et al., 2020; Cui et al., 2021; Liu et al., 2021; Han et al., 2022; Zhou et al., 2022).

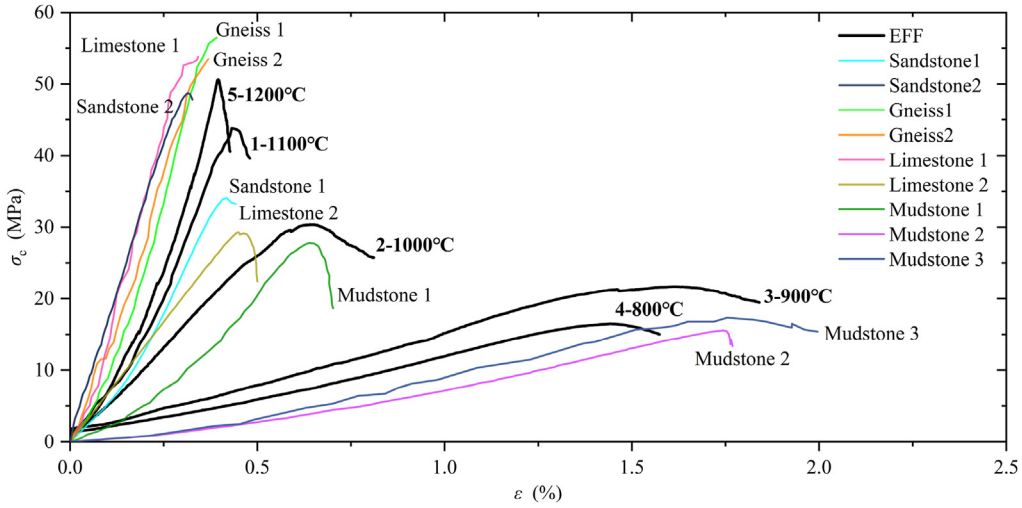

Fig. 15. Comparison of stress-strain curves between EFF specimens and natural rocks, i.e. Sandstone 1 (Du et al., 2020), Sandstone 2 (Mardalizad et al., 2018), Gneiss 1 (Zhou et al., 2022), Gneiss 2 (Agliardi et al., 2014), Limestone 1 (Walton et al., 2015), Limestone 2 (Zhang et al., 2019a), Mudstone 1 (Huang et al., 2014), Mudstone 2 (Huang et al., 2018), and Mudstone 3 (Ren et al., 2022). ε is the axial strain of the specimen.

The deformation stiffness index, defined as the ratio of the elastic modulus E to the compressive strength σ_c, is frequently used to compare the stiffness of different types of rocks (Stimpson, 1970; Shi et al., 2018). Fig. 16 compares the deformation stiffness index of EFF specimens to that of natural rocks. It can be seen that the stiffness of EFF specimens is generally similar to that of natural rocks. Nevertheless, the maximum modulus of elasticity of EFF specimens is only 13.35 GPa, which is lower than that of hard rocks.

4.6. Applicability of EFF specimens in simulating rocks

The rock type simulation undergoes a transformation from mudstone to limestone, sandstone, and finally gneiss as the temperature increases. Concurrently, a rise in sintering temperature leads to a growth in material strength, elastic modulus, brittleness, and a decrease in allowable deformation. It is noteworthy that although the strength and stress-strain curves of specimens sintered at 1200 °C closely resemble those of gneiss, the compressive strength of the specimens produced using the EFF method remains low, making them suitable for simulating soft rocks, e.g. mudstone, sandstone, and medium-hard rocks, e.g. limestone and gneiss. Through calculations using Eqs. (4)–(6), the mechanical parameter range of EFF-produced specimens can be obtained. Table 6 presents the mechanical parameters of the specimens at specific sintering temperatures and the corresponding natural rock types that they resemble.

5. Conclusions

The present study used the EFF 3D printing technique to fabricate artificial rock-like specimens and discussed the similarities to various natural rocks. The experimental result verified the feasibility of the EFF 3D printing method in fabricating artificial rocks. Based on the positive results in simulating the mechanical properties of rocks by this 3DP method, the application of this technique

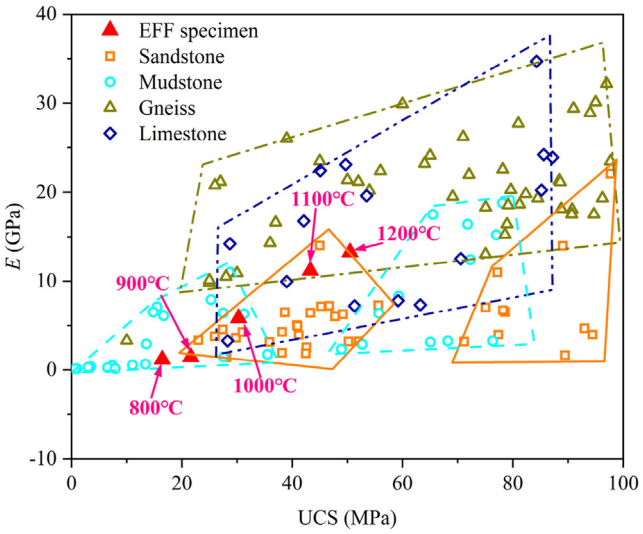

Fig. 16. Comparison of deformation stiffness between the EFF specimens and natural rocks (Data from Chen and Pan, 1998; Kahraman et al., 2000; Altindag, 2003; Hatheway, 2009; Agliardi et al., 2014; Tatone, 2014; Walton et al., 2015; Li et al., 2016; Rao and Singh, 2017; Wang et al., 2017; Geranmayeh Vaneghi et al., 2018; Zhang et al., 2019a, b; Aladejare, 2020; Cui and Gratchev, 2020; Du et al., 2020; Wang et al., 2020; Zhai et al., 2020; Cui et al., 2021; Liu et al., 2021; Han et al., 2022; Zhou et al., 2022).

Table 6
Proposed EFF specimens to simulate different natural rocks.

T (°C)	*UCS* (MPa)	*BTS* (MPa)	*E* (GPa)	Similar rock type
800–900	14.02–23.7	0–5.31	1.09–4.9	Mudstone
900–1000	23.04 –32.72	0–9.8	4.09–7.9	Sandstone, mudstone, limestone
1000 –1100	32.05 –41.74	2.42 –14.29	7.1–10.91	Sandstone, mudstone, limestone
1100 –1200	41.07 –50.76	6.91 –18.79	10.9 –13.91	Sandstone, limestone, gneiss

Note: BTS is short for Brazilian tensile strength.

in simulating the fractures or defects in rocks will be the main work in future studies. The main conclusions are listed below:

(1) The shrinkage of the EFF specimen is inevitable in the sintering process, ranging from 6% to 21%. However, the degree of contraction of the specimens in axial and radial directions is similar, and the standard specimens can be obtained by increasing the size of the specimens before sintering.
(2) The printing parameters, i.e. nozzle diameter *D*, printing layer thickness *H*, and sintering temperature *T*, all have impacts on the properties of EFF specimens and will change their physico-mechanical properties within a wide range. The effect of sintering temperature is dominant.
(3) The EFF printing material has similar mineral compositions to sedimentary rocks, both of which are mainly composed of SiO_2 and Al_2O_3, while the composition of EFF specimens can vary with the sintering temperature. The wet clay is transformed into amorphous and mullite during the sintering process, which leads to a growth in material density, strength, brittleness, and a decrease in allowable deformation.
(4) Based on the similarity analysis of failure mode, density, strength, brittleness, and stiffness between the specimens produced by EFF and natural rocks, it is recommended that specimens sintered at 800 °C-900 °C be utilized to simulate mudstone. Specimens sintered at 900 °C-1100 °C could be used to simulate sandstone, mudstone, and limestone; and specimens sintered at 1100 °C-1200 °C be employed to simulate sandstone, limestone, and gneiss.
(5) This paper conducts a preliminary study on using the EFF technology to fabricate specimens to simulate natural rocks. EFF is expected to provide a wider range of rock simulations by updating experimental instruments and changing material composition and proportions. Comprehensive investigation on more thermal-hydraulic-dynamic-mechanical properties are needed in future studies, e.g. the porosity, permeability and cracking behavior.

Declaration of competing interest

The authors declare that they have no known competing financial interests or personal relationships that could have appeared to influence the work reported in this paper.

Acknowledgments

This work was financially supported by the Beijing Natural Science Foundation for Young Scientists (Grant No. 8214052), the Talent Fund of Beijing Jiaotong University (Grant No. 2021RC226), and the State Key Laboratory for GeoMechanics and Deep Underground Engineering, China University of Mining and Technology (Grant No. SKLGDUEK2115).

References

Agliardi, F., Zanchetta, S., Crosta, G.B., 2014. Fabric controls on the brittle failure of folded gneiss and schist. Tectonophysics 637, 150–162.
Aladejare, A.E., 2020. Evaluation of empirical estimation of uniaxial compressive strength of rock using measurements from index and physical tests. J. Rock Mech. Geotech. 12, 256–268. https://doi.org/10.1016/j.jrmge.2019.08.001.
Altindag, R., 2003. Correlation of specific energy with rock brittleness concepts on rock cutting. South Afr. Inst. Min. Metall. 103, 163–171.
Altindag, R., 2010. Assessment of some brittleness indexes in rock-drilling efficiency. Rock Mech. Rock Eng. 43, 361–370.
Bobby, S.S., Singamneni, S., 2014. Influence of moisture in the gypsum moulds made by 3D printing. Procedia Eng. 97, 1618–1625.
Cao, R., Cao, P., Lin, H., Pu, C., Ou, K., 2016. Mechanical behavior of brittle rock-like specimens with pre-existing fissures under uniaxial loading: experimental studies and particle mechanics approach. Rock Mech. Rock Eng. 49, 763–783.
Chen, C.-S., Pan, E., 1998. Amadei B. Determination of deformability and tensile strength of anisotropic rock using Brazilian tests. Int J Rock Mech Min 35, 43–61. https://doi.org/10.1016/S0148-9062(97)00329-X.
Cui, C., Gratchev, I., 2020. Effects of pre-existing cracks and infillings on strength of natural rocks – cases of sandstone, argillite and basalt. J. Rock Mech. Geotech. 12, 1333–1338. https://doi.org/10.1016/j.jrmge.2020.03.008.
Cui, S., Liu, H., Meng, Y., et al., 2021. Study on fracture occurrence characteristics and wellbore stability of limestone formation. Pet. Sci. Eng. 204, 108783.
Du, B.J., Liu, C.Y., Wu, F.F., Yang, J.X., 2020. Deformation mechanism and control technology of roadway in deep mine with high stress and weak surrounding rock. Min. Saft. Eng. 37, 1123–1132. https://doi.org/10.13545/j.cnki.jmse.2020.06.006 (in Chinese).
Dursun, A.E., Gokay, M.K., 2016. Cuttability assessment of selected rocks through different brittleness values. Rock Mech. Rock Eng. 49, 1173–1190.
EFD Inc., 2003. Auger valve dispensing. https://smtnet.com/library/files/upload/EFD_-_Auger_Valve_Dispensing.pdf.
Ersoy, H., Karahan, M., Kolaylı, H., Sünnetci, M.O., 2021. Influence of mineralogical and micro-structural changes on the physical and strength properties of post-thermal-treatment clayey rocks. Rock Mech. Rock Eng. 54, 679–694.
Fang, K.T., Ge, G.N., Liu, M.Q., 2002. Uniform supersaturated design and its construction. Sci. China Ser. A-Math. 45, 1080–1088. https://doi.org/10.1007/BF02879992.
Geranmayeh Vaneghi, R., Ferdosi, B., Okoth, A.D., Kuek, B., 2018. Strength degradation of sandstone and granodiorite under uniaxial cyclic loading. J. Rock Mech. Geotech. 10, 117–126. https://doi.org/10.1016/j.jrmge.2017.09.005.
Grida, I., Evans, J.R.G., 2003. Extrusion freeforming of ceramics through fine nozzles. Eur. Ceram. Soc. 23, 629–635.
Han, D., Zhu, J., Leung, Y.-F., 2022. Failure strength and fracture characteristics of rock with discontinuity under indirect tension. J. Rock Mech. Geotech. 14, 1810–1822. https://doi.org/10.1016/j.jrmge.2022.02.007.
Hatheway, A.W., 2009. The complete ISRM suggested methods for rock characterization, testing and monitoring; 1974-2006. Environ. Eng. Geosci. 15, 47–8.

Huang, X., Liu, Q.S., Liu, B., Liu, K.D., Huang, S.B., 2014. Experimental research on the mechanical behavior of deep soft surrounding rock tunneling by TBM, 1977–86 Chin. Coal Soc. 39, 1444. https://doi.org/10.13225/j.cnki.jccs.2013 (in Chinese).
Huang, S., Wang, J., Qiu, Z., Kang, K., 2018. Effects of cyclic wetting-drying conditions on elastic modulus and compressive strength of sandstone and mudstone. Processes 6, 234. https://doi.org/10.3390/pr6120234.
Hudson, J.A., Harrison, J.P., 1997. Engineering Rock Mechanics. Elsevier Science, Amsterdam, Netherlands. https://doi.org/10.1016/B978-0-08-043864-1.X5000-9.
Ishutov, S., Hasiuk, F.J., Harding, C., Gray, J.N., 2015. 3D printing sandstone porosity models. Interpretation. https://doi.org/10.1190/INT-2014-0266.1.
Jaber, J., Conin, M., Deck, O., et al., 2020. Investigation of the mechanical behavior of 3D printed polyamide-12 joints for reduced scale models of rock mass. Rock Mech. Rock Eng. 53, 2687–2705.
Jiang, C., Zhao, G.-F., 2015. A preliminary study of 3D printing on rock mechanics. Rock Mech. Rock Eng. 48, 1041–1050.
Jiang, Q., Feng, X., Gong, Y., T, E., 2016a. Reverse modelling of natural rock joints using 3D scanning and 3D printing. Comput. Geotech. 73, 210–220.
Jiang, C., Zhao, G.-F., Zhu, J., Zhao, Y.-X., Shen, L., 2016b. Investigation of dynamic crack coalescence using a gypsum-like 3D printing material. Rock Mech. Rock Eng. 49, 3983–3998.
Jiang, Q., Liu, X., Yan, F., et al., 2021. Failure performance of 3DP physical twin-tunnel model and corresponding safety factor evaluation. Rock Mech. Rock Eng. 54, 109–128.
Ju, Y., Xie, H., Zheng, Z., et al., 2014. Visualization of the complex structure and stress field inside rock by means of 3D printing technology. Chin. Sci. Bull. 59, 5354–5365. https://doi.org/10.1007/s11434-014-0579-9.
Kahraman, S., Balcı, C., Yazıcı, S., Bilgin, N., 2000. Prediction of the penetration rate of rotary blast hole drills using a new drillability index. Int. J. Rock Mech. Min. 37, 729–743.
Li, H.M., Li, H.G., Song, G.J., Wang, K.L., 2016. Petrophysical and mechanical properties of coal measures strata in Shendong mining area. Chin. Coal Soc. 41, 2661–2671. https://doi.org/10.13225/j.cnki.jccs.2016.1218 (in Chinese).
Liu, H.B., Zhan, Y.X., Jiang, Y.D., Wang, Z.H., 2017. Experimental study on mechanical properties of 3D printed gypsum sample. Mech. Eng. 39, 455–459, 471.
Liu, H., Zhu, C., Zheng, K., Ma, C., Yi, M., 2021. Crack initiation and damage evolution of micritized framework reef limestone in the South China Sea. Rock Mech. Rock Eng. 54, 5591–5601.
Lowmunkong, R., Sohmura, T., Suzuki, Y., Matsuya, S., Ishikawa, K., 2009. Fabrication of freeform bone-filling calcium phosphate ceramics by gypsum 3D printing method. Biomed. Mater. Res. B Appl. Biomater. 90B, 531–539.
Mardalizad, A., Scazzosi, R., Manes, A., Giglio, M., 2018. Testing and numerical simulation of a medium strength rock material under unconfined compression loading. J. Rock Mech. Geotech. 10, 197–211. https://doi.org/10.1016/j.jrmge.2017.11.009.
Moon, S.K., Tan, Y.E., Hwang, J., 2014. Yoon Y-J. Application of 3D printing technology for designing light-weight unmanned aerial vehicle wing structures. Int. J. Pr. Eng. Man. GT. 1, 223–228.
Noferesti, H., Rao, K.S., 2010. New observations on the brittle failure process of simulated crystalline rocks. Rock Mech. Rock Eng. 43, 135–150.
Pettijohn, F.J., 1975. Sedimentary Rocks. Horper and Row Publishers, New York, England.
Pollard, D.D., Aydin, A., 1988. Progress in understanding jointing over the past century. Geol. Soc. Am. Bull. 100, 1181–1204.
Rao, K.S., Singh, T., 2017. Two-dimensional finite element based parametric analysis of south portal slope, Rohtang Tunnel, India. Procedia Eng. 173, 1330–1333.
Ren, M., Wu, X., Zhang, L., Pan, J., Li, N., 2022. Study on mechanical properties and nonlinear strength model of deep water-sensitive rock in xianglu mountain tunnel. Geofluids 2022, 1–23. https://doi.org/10.1155/2022/8398602.
Rimsaite, J., 1979. Natural amorphous materials, their origin and identification procedures. Dev. Sedimentol. 567–576. https://doi.org/10.1016/S0070-4571(08)70755-6.
Shi, X.M., Liu, B.G., Xiang, Y.Y., Qi, Y., 2018. A method for selecting similar materials for rocks in scaled physical modeling tests. J. Min. Sci. 54, 938–948. https://doi.org/10.1134/S1062739118065084.
Song, L., Jiang, Q., Shi, Y.-E., et al., 2018. Feasibility investigation of 3D printing technology for geotechnical physical models: study of tunnels. Rock Mech. Rock Eng. 51, 2617–2637.
Song, R., Wang, Y., Ishutov, S., et al., 2020. A comprehensive experimental study on mechanical behavior, microstructure and transport properties of 3D-printed rock analogs. Rock Mech. Rock Eng. 53, 5745–5765.
Stimpson, B., 1970. Modelling materials for engineering rock mechanics. Int. J. Rock Mech. Min. 7, 77–121.
Tan, W.-H., Ba, J., Guo, M.-Q., et al., 2018. Brittleness characteristics of tight oil siltstones. Appl. Geophys. 15, 175–187.
Tatone, B., 2014. Investigating the Evolution of Rock Discontinuity Asperity Degradation and Void Space Morphology under Direct Shear. PhD Thesis. University of Toronto, Canada.
Walton, G., Arzúa, J., Alejano, L.R., Diederichs, M.S., 2015. A laboratory-testing-based study on the strength, deformability, and dilatancy of carbonate rocks at low confinement. Rock Mech. Rock Eng. 48, 941–958.
Wang, H.W., Li, J.T., Gao, J.C., Lin, H., 2017. Tensile strength of slates under dry and saturated conditions based on Brazilian splitting method. J. Cent. South Univ. 48, 1044–1048.
Wang, Z., Yang, S., Tang, Y., 2020. Mechanical behavior of different sedimentary rocks in the Brazilian test. Bull. Eng. Geol. Environ. 79, 5415–5432. https://doi.org/10.1007/s10064-020-01906-8.
Xiong, Z.Q., Jiang, Q., Gong, Y.H., Song, L.B., Cui, J., 2015. A method for preparing natural joints of rock mass based on 3D scanning and printing techniques and its experimental validation. Rock Soil Mech. 36, 1557–1565.
Yagiz, S., Yazitova, A., Karahan, H., 2020. Application of differential evolution algorithm and comparing its performance with literature to predict rock brittleness for excavatability. Int. J. Min. Reclamat. Environ. 34, 672–685.
Zhai, S., Su, G., Yin, S., Zhao, B., Yan, L., 2020. Rockburst characteristics of several hard brittle rocks: a true triaxial experimental study. J. Rock Mech. Geotech. 12, 279–296. https://doi.org/10.1016/j.jrmge.2019.07.013.
Zhang, J., Yao, D.X., Lu, H.F., Xu, Z.D., 2019a. Characteristics and statistical analysis of physical and mechanical parameters of coal measure rock mass: a case study of Qingdong coal mine in northern Anhui Province. J. Longyan Univ. 37, 39–49. https://doi.org/10.16813/j.cnki.cn35-1286/g4.2019.02.008 (in Chinese).
Zhang, Y., Zuo, S., Yu, B., Chen, S., Jia, J., 2019b. Study on bending damage constitutive model and mechanical properties of limestone based on acoustic emission. Adv. Civ. Eng. 2019, 1–10.
Zhao, Y., Zhang, L., Wang, W., et al., 2016. Cracking and stress–strain behavior of rock-like material containing two flaws under uniaxial compression. Rock Mech. Rock Eng. 49, 2665–2687.
Zhou, T., Zhu, J.B., 2018. Identification of a suitable 3D printing material for mimicking brittle and hard rocks and its brittleness enhancements. Rock Mech. Rock Eng. 51, 765–777.
Zhou, T., Zhu, J., Xie, H., 2020. Mechanical and volumetric fracturing behaviour of three-dimensional printing rock-like samples under dynamic loading. Rock Mech. Rock Eng. 53, 2855–2864.
Zhou, Y., Liu, X., Li, X., 2022. Progressive failure process of anisotropic rock: insight from full-field strain evolution. KSCE J. Civ. Eng. 26, 460–471.
Zou, C., Yingying, S., Liu, K., Cheng, Y., Li, J., 2022. Feasibility of artificial materials in simulating rock failure based on rate-dependent brittleness indexes. Rock Mech. Rock Eng. 55, 4999–5027.

Dr. Xiaomeng Shi is currently working as a lecture at Beijing Jiaotong University. He obtained his PhD in Geotechnical Engineering from Beijing Jiaotong University, and worked as a postdoctoral fellow at Tsinghua University and Monash University. His research focuses mostly on the rock mechanics and rock engineering.